Journal of Photochemistry and Photobiology A: Chemistry 207 (2009) 126–134

Contents lists available at ScienceDirect

Journal of Photochemistry and Photobiology A: Chemistry

journal homepage: www.elsevier.com/locate/jphotochem

Nano-textured metallic surfaces for optical sensing and detection applications

Yukie Yokota [a], Kosei Ueno [a,b], Saulius Juodkazis [a], Vygantas Mizeikis [a], Naoki Murazawa [a], Hiroaki Misawa [a,*], Haruya Kasa [c], Kenji Kintaka [c], Junji Nishii [c]

[a] Research Institute for Electronic Science, Hokkaido University, Kita 21 Nishi 10, CRIS Bldg., Sapporo 001-0021, Japan
[b] PRESTO, Japan Science and Technology Agency, Kawaguchi 332-0012, Japan
[c] Photonics Research Institute, National Institute of Advanced Industrial Science and Technology, 1-8-31 Midorigaoka, Ikeda, Osaka 563-8577, Japan

ARTICLE INFO

Article history:
Available online 19 October 2008

Keywords:
Metallic nano-structures
Plasmon
Surface-enhanced Raman scattering
Holographic lithography
Laser processing

ABSTRACT

This work describes fabrication of three-dimensionally nano-textured silicon surface structures metalized by thin gold films, and their application for optical sensing and detection of solute molecules utilizing surface-enhanced Raman scattering (SERS) effect. Two types of sensitive surfaces were prepared by different techniques. The first of them was a checkerboard pattern of 3D nanoblocks defined in compact areas on the surface of a silicon wafer using highly accurate electron-beam lithography (EBL) technique, and fabricated by dry reactive-ion etching (RIE) technique with subsequent metalization of the surface by gold sputtering. The second type of sensitive surface consisted of a square array of nano-apertures, defined on a large area of the silicon surface by a less accurate but simpler ultraviolet holographic lithography, and subsequently fabricated in a sequence of dry and wet etching as well as gold sputtering steps. The fabricated structures were found to exhibit significant near-field enhancement, as evidenced by strong SERS signal from the sensors immersed in aqueous pyridine solutions with concentrations as low as 10^{-9} M due to the presence of well-defined 3D periodic texture of the structure.

1. Introduction

Tailoring of optical fields in nanoscale spatial domains, which is possible by exploiting surface plasmons [1,2], has attracted attention in various fields of science and technology, including development of optical environmental sensors and detectors [3–5]. In advanced optical sensing and detection applications, high sensitivity, spectral selectivity, and spatial resolution become increasingly important. In order to answer these demands, non-linear optical interactions become widely used, since optical non-linearities are often highly sensitive to the local environment, and can provide non-linear scaling of measurable optical quantities (such as the yield of fluorescence or harmonics generation) with intensity of the incident probing radiation. High incident intensity or irradiance levels required for optical non-linearities can be achieved by the use of ultra-short laser pulses and their tight focusing in the target environment. Since field enhancement achievable by ordinary focusing is inherently limited by diffraction, the possibility of circumventing this limitation by using specially tailored photonic crystals or microcavities, as well as quantum-optical effects have attracted significant interest [6]. Recently, "super-focusing" of the optical radiation into sub-wavelength, nanoscale domains due to surface plasmons has become increasingly widely used for enhancing the local optical field intensity [7–9]. Field enhancement via concentration in sub-wavelength spatial regions can be especially efficient using surface plasmons localized at the surface of metallic nano-particles or nano-structured surfaces. The enhanced field can easily induce optical non-linearities in materials occupying the high-field regions. These non-linearities often reflect properties of the material, thus allowing environmental optical sensing and detection. Among various metallic systems (surfaces, films, nano-structures), a relevant example for this study is a nano-sphere in vacuum. Local field amplitude inside the nano-sphere can be found from electrostatic approximation [1]:

$$E_{\mathrm{loc}} = \frac{3}{\varepsilon_{\mathrm{m}}(\omega) + 2} E_0, \tag{1}$$

where E_0 is the amplitude of the incident field, ω is the cyclic frequency of light, and $\varepsilon_{\mathrm{m}}(\omega)$ is the complex dielectric function of metal. The local field amplitude enhancement factor is expressed as $L(\omega) = 3/(\varepsilon_{\mathrm{m}}(\omega) + 2)$. Noble metals, such as Au, Ag, and Cu, have high density of free electrons, low dissipative losses, and their dielectric function has negative real part and negligible imaginary part in a wide spectral range. It is easy to see from Eq. (1) that $L(\omega) > 1$ is obtained in these circumstances.

* Corresponding author. Tel.: +81 11 706 9358.
E-mail address: misawa@es.hokudai.ac.jp (H. Misawa).

1010-6030/$ – see front matter © 2008 Elsevier B.V. All rights reserved.
doi:10.1016/j.jphotochem.2008.10.007

Artificial engineering of metallic surfaces, interfaces, and thin films allows one achieve geometries of nano-particles that provide field intensity enhancement factors in excess of 10^3 (intensity I of the incident optical radiation, which is measured in the units of [W/cm^2] is proportional to the square of the electric field amplitude $I \sim E^2$). Nano-engineering of metals using techniques borrowed from semiconductor micro- and nano-processing industry, allow precise control of the geometry with accuracy of up to a few nanometers. With adequate theoretical understanding about factors defining spatial and spectral concentration of plasmonic near-field, one can design and fabricate plasmonic nano-structures with required characteristics. For example, using precisely tailored nano-antennae consisting of pairs of closely spaced gold nano-particles, field concentration and intensity enhancement in the separating nanogaps may become enhanced to the level where non-linear absorption is induced in the nanogaps even by low-intensity irradiation of an incoherent thermal lamp source. Using the lamp excitation and the plasmonic field enhancement it was possible to demonstrate photo-polymerization reaction triggered by a weak thermal source in a commercial photoresist [8]. Without the field enhancement, irradiation by powerful coherent light sources, such as pulsed ultrafast lasers, is normally required for observable non-linearities to occur. Plasmonic nano-structures made of gold or other noble metals can be used for functionalization of surfaces for sensor-based applications, whose operation is based on strongly localized light-matter interactions, such as surface-enhanced Raman scattering (SERS) and surface-enhanced resonant Raman scattering (SERRS) effects. This effect is typically observed in liquid solutions containing various molecular and ionic species that are adsorbed on disordered or periodically structured surface of Au, Ag, and Cu. The adsorbed molecules are subjected to enhanced electromagnetic field, and their vibrational modes contribute to strong Raman scattering [10]. In addition, charge-transfer between the surface and analyte molecules may occur in resonance with the external excitation, contributing to the strength of SERS signal. Enhancement of the Raman signal by factors of up to 10^{14}–10^{15} can be reached [11], and observation of single-molecule Raman scattering [12,13] is possible.

SERS enhancement has become increasingly widely employed for plasmonic sensing. Simplest SERS sensors exploit plasmons propagating at smooth metallic surface [14]. Recently, much attention was focused on SERS application plasmons localized on disordered metallic nano-structures prepared by a wide variety of available chemical techniques [3–5,15]. In order to generate spatially and spectrally homogeneous SERS response, large area well-ordered nano-structured substrates are needed. Since precise nano-structuring of materials is a challenging task, various techniques were developed for this purpose. One of the most popular approaches is based on deposition of metallic films on surfaces templated (masked) by nano-spheres [16,17], which leads to creation of periodically structured films. The alignment of nano-spheres can be improved using pits additionally fabricated on flat substrates by dry etching [18]. Recently, three-dimensionally structured metallic surfaces for SERS were prepared by depositing gold over an ordered monolayer of nano-spheres [19], and by metalization of surfaces containing pyramidal pits fabricated by anisotropic wet etching [20]. The main challenge arising with well-ordered, precisely tailored structures lies in the fact that in order to augment large SERS signals, structures comprised of many closely packed active regions exhibiting similar field enhancement characteristics are needed. However, when geometry of the materials and interfaces is optimized for the required spectral range, the dense packing condition cannot always be met. Likewise, if the close-packing property is optimized, near-field coupling effects such as dipole and multipole interactions between the closely spaced nano-particles may modify the spectral response and the field enhancement factor. Thus, it is generally difficult to tailor the structures to fully satisfy all the conflicting requirements simultaneously.

Properties and applications of plasmonic nano-structures for optical sensing and detection, as well as solutions that can help in alleviating the above described problems are the main focus of this work. In particular, we describe preparation of optical sensors using two different approaches. The first approach is based on preparation of small-area plasmonic sensors in which nano-particles are defined with very high resolution using electron-beam lithography (EBL). The second approach is based on fast, but less accurate prototyping of large-area metallic nano-structures using optical holographic technique. Both approaches have advantages and disadvantages, and both are important from the practical viewpoint. Small sensors with total active area not exceeding 100 μm × 100 μm can be tailored using the first method with high accuracy, and their parameters can be controlled more precisely. However, if their small area (or number of active regions) still limits the total sensitivity, and compact size of the sensor is not an issue, integral sensitivity can be boosted by increasing the sensor area. Using the second technique, sensors with areas up to 1 cm × 1 cm can be prepared, and the larger area may compensate the negative effects of lower fidelity of the fabrication technique.

2. Samples, their fabrication and characterization

2.1. High-resolution fabrication of small-area 3D textured surfaces

High-resolution fabrication of 3D nano-structured metalized surfaces was carried out by essentially the same procedures as those used in our earlier work for the preparation of planar metallic nano-structures [21]. The main modification applied in this work was the addition of dry etching by inductively coupled ion plasma, and ashing in O_2 in order to obtain 3D surface nano-structuring. The sample preparation procedure is explained schematically in Fig. 1. First, planar pattern corresponding to the footprint of the desired 3D structure (its geometry will be specified later) was defined by EBL in a thin film of co-polymer resist (ZEP-520a, Zeon Co., Ltd., Tokyo, Japan) spin-coated on Si wafers. For EBL, a high-resolution EBL system (ELS-7700H, Elionix Co., Ltd., Japan) operating at a 100-kV accelerating voltage was used. EBL was carried out at an exposure dose of 1.2 C/cm^2, and electrical current of 5 pA. The structures occupy an area of about 30 μm × 30 μm (although the maximum total area that can be patterned by the EBL machine is 1 cm × 1 cm). Resolution of EBL writing is in the range of a few nanometers, as confirmed in earlier experiments [22]. The exposed films were developed in a standard developer (Zeon Co., Ltd., Japan). Afterwards, dry etching and ashing were applied in order to obtain patterns of about 100 nm deep pits on the silicon surface. The dry plasma etching was carried out in a SF_6 gas for 1.5 min at 90 cm^3/min flow; while 50 cm^3/min flow of a C_4F_8 gas was used to protect vertical walls from under-etching. The ashing was carried out in a 40-cm^3/min flow of O_2 for 2 min. The etched surface was subsequently sputtered by a 40-nm gold layer (using MPS-4000, ULVAC, Japan).

The fabricated samples were inspected by scanning electron microscopy (SEM) without depositing any additional conductive coating in order to resolve lateral patterns of the structures. These observations have confirmed that the final 3D metalized patterns were highly uniform, in accordance to the results of our earlier studies carried on similar structures [7,21–24]. SEM images of two fabricated structures are presented in Fig. 2. The chosen geometry

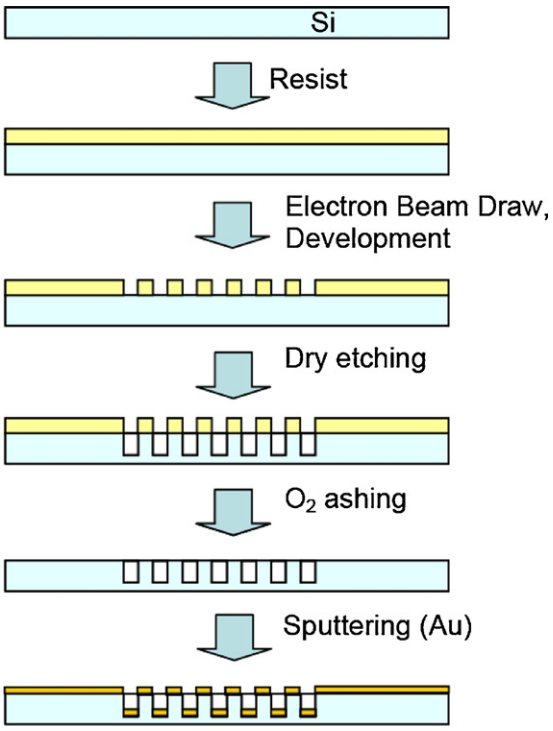

Fig. 1. Preparation of reusable 3D textured silicon surface by EBL and dry-etching techniques, and its metalization by Au sputtering.

of the samples can be described as a checkerboard pattern of 3D silicon nanoblocks having a gold film deposited on all horizontal surfaces, and bare (or nearly bare) side walls. Schematic depiction of this geometry can be found in Fig. 7. The samples shown in Fig. 2 consist of nanoblocks with side length of 100 and 150 nm and a uniform height of 100 nm. Thickness of the gold film on the horizontal surfaces is 40 nm. Despite some non-parallelism of the side walls of the blocks, the images illustrate high resolution of the fabrication achieved.

2.2. Fabrication of large-area 3D structured surfaces by holographic technique

Like the fabrication procedures described above, fabrication of large area plasmonic sensors was aimed at obtaining metalized 3D nanopatterned surface structures. However, the fabrication process and the geometry of the structures were different. In this case, instead of using EBL for the definition of 2D footprint of the structure on silicon surface, faster (but less accurate) prototyping of the pattern was done using interference lithography technique. The initial samples prepared for lithography consisted of Si wafers coated by 100-nm thick silica (SiO_2) film with fluorine (F_2) doping level varying from 6.353 mol% at the Si/SiO_2 interface to zero at the 50 nm depth (hence, the top 50 nm thickness of the film was undoped SiO_2). The coating was done by "plasma-enhanced" chemical vapor deposition (PECVD) technique. On these substrates, 500 nm thick positive resist (TDMR-AR80 HP, Tokyo Ohka Kogyo Co., Ltd.) was deposited, enclosed at both interfaces by two 100 nm thick anti-reflection films. Holographic definition of the resist mask was conducted in an area having 2 cm diameter by two-step exposure to an interference field formed by two expanded, spatially filtered, and collimated continuous-wave (cw) HeCd laser beams with 325 nm wavelength. The principle and implementation of holographic lithography is shown in Fig. 3. Two identical beams were produced by diffraction on a phase mask, and overlapped on the exposure region at a mutual angle of 33°, resulting in 2D interference fringe pattern with the period of 300 nm. The two exposure steps were identical, except for the substrate orientation, which was rotated by the 90° angle about normal to its surface between the exposures. The resulting exposure pattern can be described by a

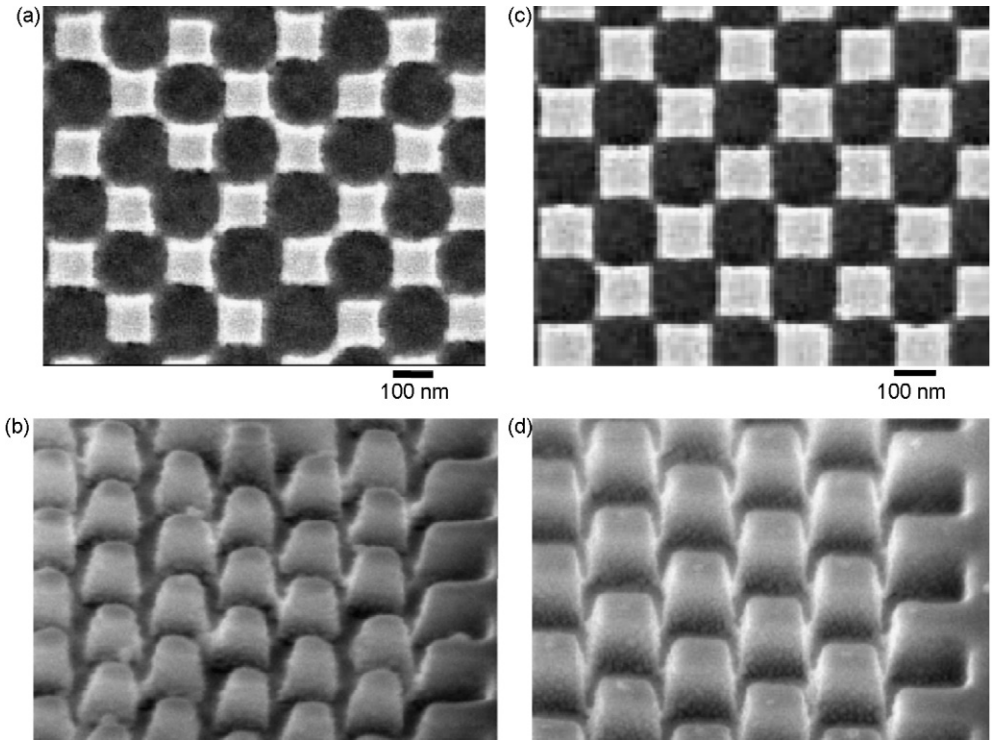

Fig. 2. Top (a and c) and corresponding perspective view (b and d) SEM images of nano-textured Si surface consisting of nanoblocks with 100 and 150 nm side-lengths. The nanoblock height (dry-etching depth) is 100 nm; thickness of the gold film sputtered on the surface is 40 nm.

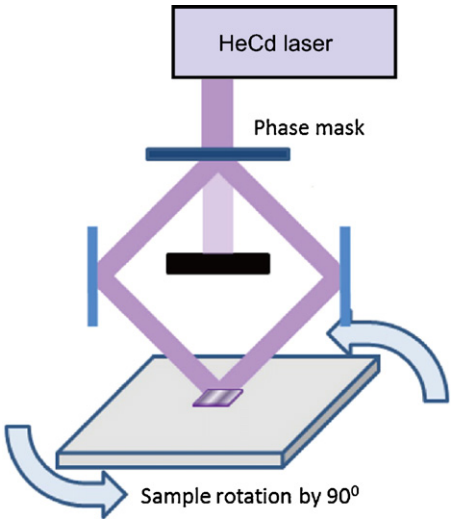

Fig. 3. Definition of photoresist mask using two-step holographic lithography technique.

2D periodic lattice of holes; hole diameter of about 150 nm was achieved.

The complete sequence of sample fabrication and processing steps is depicted schematically Fig. 4. The exposed (1) and developed (2) structures were subsequently dry etched in order to remove SiO_2 (3), and anti-reflection layers and resist (4). Next, wet

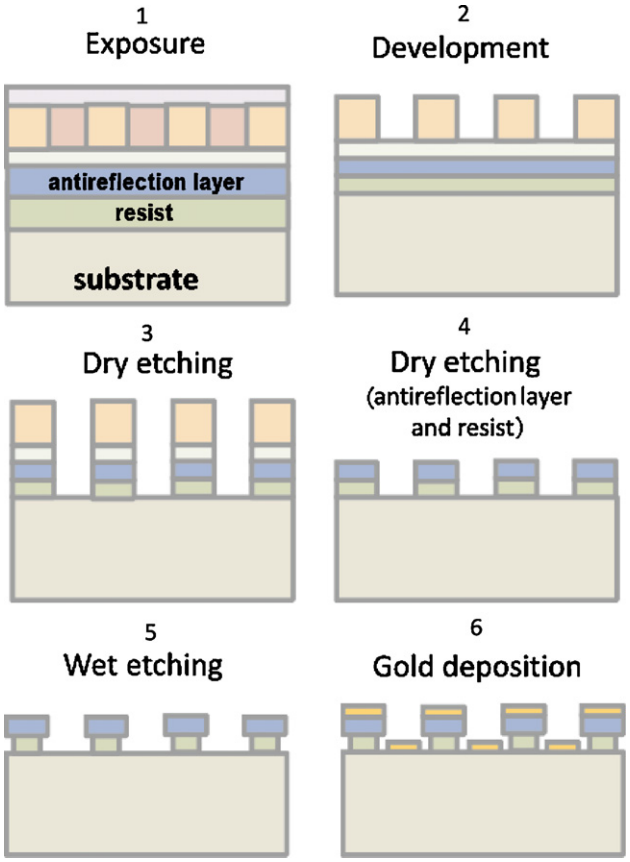

Fig. 4. Preparation of reusable 3D textured silicon surface by holographic lithography, etching, and metalization by gold. Note: step (4) is a simplified representation of three separate dry-etching steps which were needed for the complete removal of two anti-reflection layers and one photoresist layer.

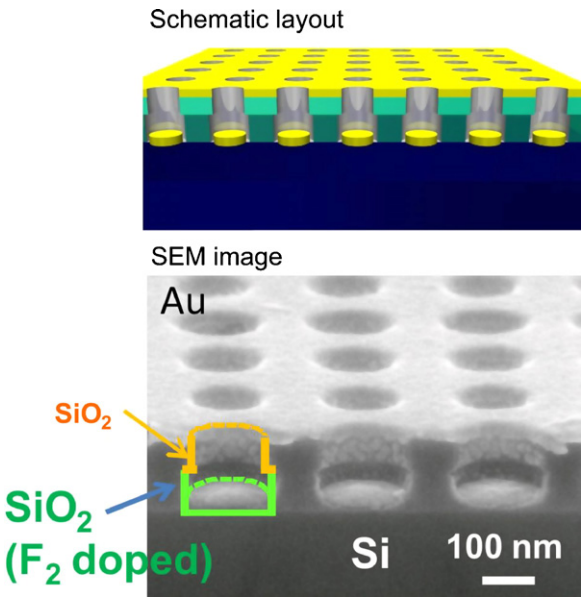

Fig. 5. Schematic layout of 3D patterned surface structures metalized by thin gold films obtained using the procedures outlined in Fig. 4, and cross-sectional view SEM image of the fabricated structure.

etching of the samples in 5 wt% HF aqueous solution was carried out at room conditions (5). The etching rate of F_2-doped silica was 270 nm/min (4.2 times larger than that of pure silica) and resulted in under-etched structures [25]. Then, gold deposition (6) by sputtering was carried out over the entire patterned area of 2 cm diameter.

These fabrication steps resulted in 3D textured surface structures whose schematic layout and SEM image are depicted in Fig. 5. These structures can also be recycled using gold removal and re-sputtering steps as described in the previous section.

2.3. Characterization of plasmonic and optical sensing properties

Optical properties of the fabricated samples were initially characterized by measuring their optical extinction spectra. This was accomplished using a variety of homemade and commercially available experimental setups. At visible wavelengths, extinction measurements were conducted in transmission geometry using optical setup assembled on an inverted optical microscope, and described in some detail in our previous report [21]. The microscope was mainly needed in order to be able to characterize small samples (or small parts of larger samples). In the near-infrared wavelength range, extinction spectra were measured using a commercially available Fourier-transform infrared (FT-IR) spectrometer equipped with a microscope attachment (FT-IR, IRT-3000, Jasco, Japan). This setup enabled reliable measurements in the wavelength range of about 670–3000 nm from areas of about 20 μm × 20 μm on the samples.

Optical setup used for Raman measurements is schematically shown in Fig. 6(a). Raman scattering spectra were measured using homemade setup assembled on a microscope (BX51, Olympus, Japan), and a solid state cw laser (CrystaLaser) excitation source at the wavelength of 785 nm. The laser beam was coupled into the microscope and focused on the sample by a water-immersion 100× magnification objective lens with a numerical aperture of NA = 1.0. Raman signal was collected in reflection geometry by the same microscope lens, and coupled into a side-port of the microscope. Subsequently, the signal was spectrally resolved using SpectraPro 300i (Acton Research) spectrometer, and recorded using a liquid nitrogen-cooled CCD camera. To test the Raman detection, we have

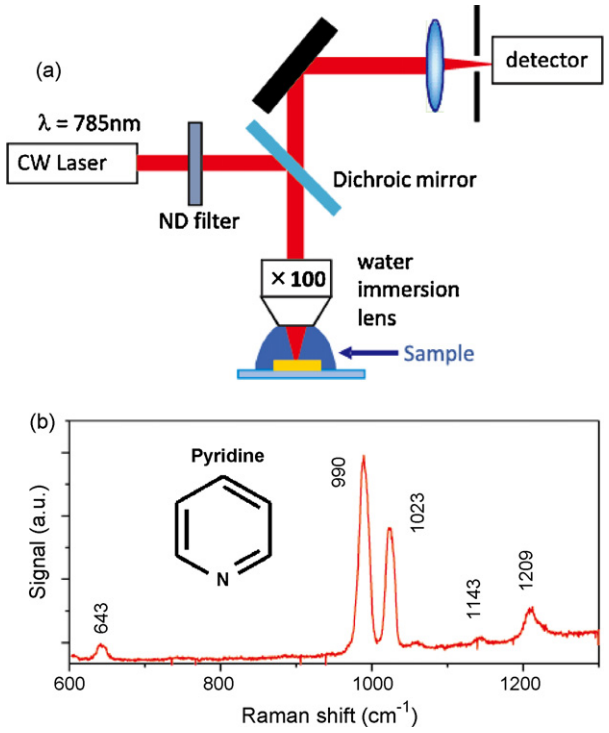

Fig. 6. Optical setup for the measurements of Raman spectra (a), Raman spectrum of pyridine solution (b).

used bulk pyridine (Wako) solution. Typical liquid Raman spectrum of pyridine is shown in Fig. 6(b). Pyridine molecules are known to be highly SERS active, and are widely used in SERS studies. As can be seen from the figure, bulk pyridine exhibits two well-pronounced Raman bands at 990 and 1023 cm^{-1}. Spectral positions of these bands allow their identification as the totally symmetric ring breathing modes ν_9 and ν_8 according to the available literature [26,27]. In the following, we will mainly focus on the SERS signal occurring in vicinity of these lines (which exhibit slight spectral shifts due to adsorption of molecules on metallic surface [14,28]).

2.4. Theoretical characterization by FDTD calculations

Theoretical interpretation of surface plasmons localized on metallic structures is well-developed, and various descriptions have been widely available in the existing literature [1,29]. Generally, classical electrodynamics is sufficient for adequate description of plasmonic phenomena. Hence, these interpretations are free from quantum uncertainties, and are in principle perfectly accurate. However, analytical descriptions are only available for simplest geometries, such as surfaces [29] or ellipsoidal nano-particles [30,31]. In these circumstances, numerical modeling become valuable for the exploration of plasmonic properties of nano-particles unrestricted by their shapes, sizes and surrounding environments. Most numerical modeling techniques are based on the solution of Maxwell's equations. In this work we use Finite-Difference Time-Domain (FDTD) technique [32] for numerical studies. FDTD is perhaps the most straightforward numerical method, in which temporal evolution of an initial optical field is calculated directly without any simplifying assumptions or approximations, and from that evolution optical properties (e.g., optical extinction) and spatial field distribution patterns can be deduced.

In this study, FDTD calculations were performed using commercially available FDTD Solutions software package (Lumerical, Inc.). The calculations were conducted as follows. Spatial FDTD domain containing unit cell (the smallest geometrically unique fragment of the structure), was discretized on a rectangular grid with variable discretization step set to vary within the range from 1.5 to 5 nm. At the boundaries of the FDTD domain appropriate boundary conditions were defined (both perfectly matched layer and periodic boundary conditions were used). Geometric shapes of nano-structures were defined as close as possible to those of the actual samples. Dielectric dispersion of gold was described using plasma and Drude approximation of experimental dependencies known from the literature [33,34]. Silicon substrate was assumed to have a constant refractive index of $n = 3.4$. During the calculations, short optical pulse spectrally spanning the entire spectral range of interest was launched into the FDTD domain. Subsequently, the field was advanced in space and time in small steps according to the Maxwell's equations, simultaneously monitoring flows of optical power in and out of the FDTD region. After elapsing a time sufficient for all excitations in the FDTD domain to fully decay, the calculations were terminated, and the monitored temporal dependencies were Fourier-transformed in order to obtain spectral dependencies of the scattered, and absorbed fields. So called Total-Field Scattered-Field (TFSF) method [32] was used in determining the scattering parameters. Subsequently, spatial maps of the field intensity were extracted from the calculations at the wavelengths of interest. In the calculations, $E = 1$ initial field amplitude was assumed. Thus, the calculated field intensity maps represent the field intensity enhancement factor.

3. Utilization of surface-enhanced Raman scattering for optical sensing

This section describes application of the structures described in Sections 2.1 and 2.2 for optical sensing applications. The sensing is based on the detection of SERS signal induced via the optical near-field in adsorbed pyridine molecules.

3.1. High-resolution, small-area 3D textured surface structures

For experimental demonstration that 3D nano-textured and gold-coated silicon surface described in Section 2.1 is prospective for sensitive detection of Raman-active molecules, the samples were immersed in pyridine solutions of various concentrations, and Raman signal intensity was measured under different excitation conditions using the setup described in Section 2.3. Prior to description of the experimental results, it is instructive to briefly consider theoretical near-field intensity patterns calculated using FDTD technique. Fig. 7 shows schematic layout of the 3D nano-structured silicon surface metalized by thin gold film, which was used as the model for the FDTD calculations (see Section 2.4 for other details). In order to qualitatively estimate possible effects of side-wall coating by gold on the near-field enhancement, FDTD simulations were carried out for both bare and coated side-walls, as is illustrated in the sketches in Fig. 7(a and b). Monitoring field enhancement in the full 3D computational FDTD domain is possible, but difficult due to excessive memory requirement by the calculations. Nevertheless, even a simpler monitoring of the field in selected 2D planes can reveal the potential of structures as field enhancers. Field intensity enhancement patterns in Fig. 7 are taken on horizontal planes that cut though half-height of the silicon blocks constituting the 3D checkerboard structure. These patterns are obtained when the incident optical wave is polarized linearly along the diagonal of the checkerboard pattern. It was demonstrated earlier, that in 2D checkerboard patterns consisting of gold nanoblocks deposited on flat substrates, orientation of polarization along the diagonal leads to strong localization of the near-field at

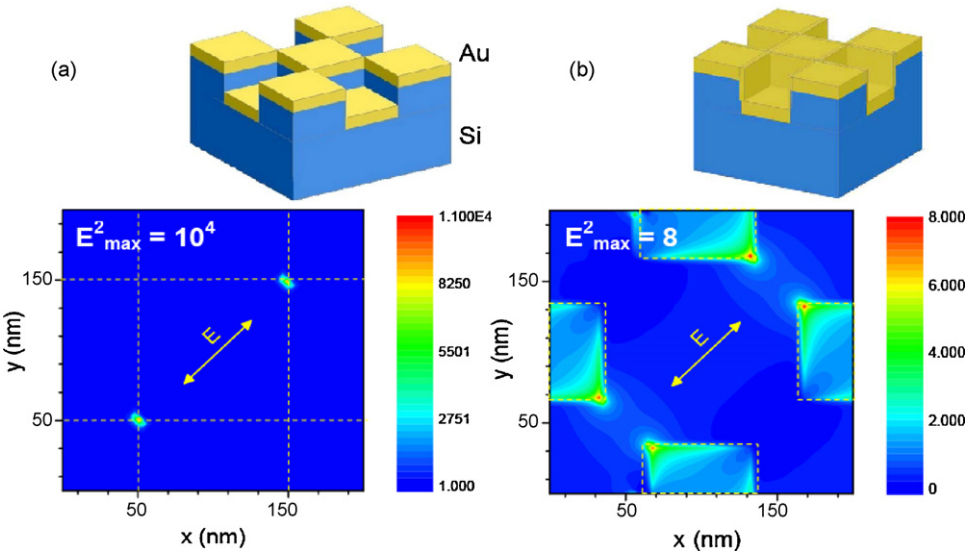

Fig. 7. Spatial maps of the near-field intensity enhancement factor calculated at the excitation laser wavelength ($\lambda = 780$ nm) for 3D textured silicon surface coated by 40-nm thick gold layer on horizontal surfaces only (a), and for additional coating of side walls by 15-nm thick gold film (b). The maps were taken on x–y planes that cut through the half-height of the silicon blocks. In the calculations, linear polarization of the source was oriented along the diagonal of the checkerboard pattern as illustrated by the arrows. The calculations were done assuming periodic boundary conditions.

the necks between the nanoblocks [7,8]. Since footprints of our 3D structures have the same symmetry as those of 2D checkerboard patterns, it is obvious that diagonal orientation of the polarization is preferable for maximizing the field enhancement. On the other hand, more detailed theoretical studies are needed in order to clarify the role of polarization and other factors, such as thickness of the Au film. As can be seen from Fig. 7(a), in the case of 3D checkerboard patterns, intensity enhancement by the factor up to 10^4 can be expected on the 3D textured surface with bare side walls. In this layout, the field is predominantly concentrated in the narrow necks between the neighboring blocks. The displayed region contains two "hot spots" aligned parallel to the polarization of the excitation source. Since FDTD calculations were performed assuming periodic boundary conditions, in extended 3D surfaces, the "hot spots" would form lines along the polarization direction. It can be thus concluded that in the structure shown in Fig. 7(a), various optical non-linearities, such as SERS effect, will predominantly occur in these periodically arranged "hot spots". Fig. 7(b) demonstrates that partial coating of the side surfaces by gold creates unfavorable conditions for the field enhancement, which becomes reduced to the factor of 8. As the patterns shown in Fig. 7(a and b) are calculated for single planes, one can expect a higher enhancement to be present on other planes; however, drastic differences from the calculated values are unlikely.

Fig. 8(a) shows experimental spectra of Raman scattering measured from the 3D structured sample immersed in a pyridine solution having the concentration of 10^{-4} M at various laser power levels. As can be seen, Raman peak centered near 1014 cm^{-1} becomes detectable above the 8.3 W/cm^2 laser power level. As no signal could be observed from bulk pyridine solution at same excitation levels, we assume that near-field enhancement plays crucial role for the observed Raman signal. Fig. 8(b) summarizes the Raman peak intensity versus the incident laser powers dependence. The observed linear power dependence can be expected, since according to the literature [1], scattered power due to spontaneous Raman scattering, $P_{SC}(\omega_R)$, at the cyclic frequency, ω_R is

$$P_{SC}(\omega_R) = N\sigma_{SERS}L(\omega_R)^2L(\omega_I)^2I(\omega_I), \quad (2)$$

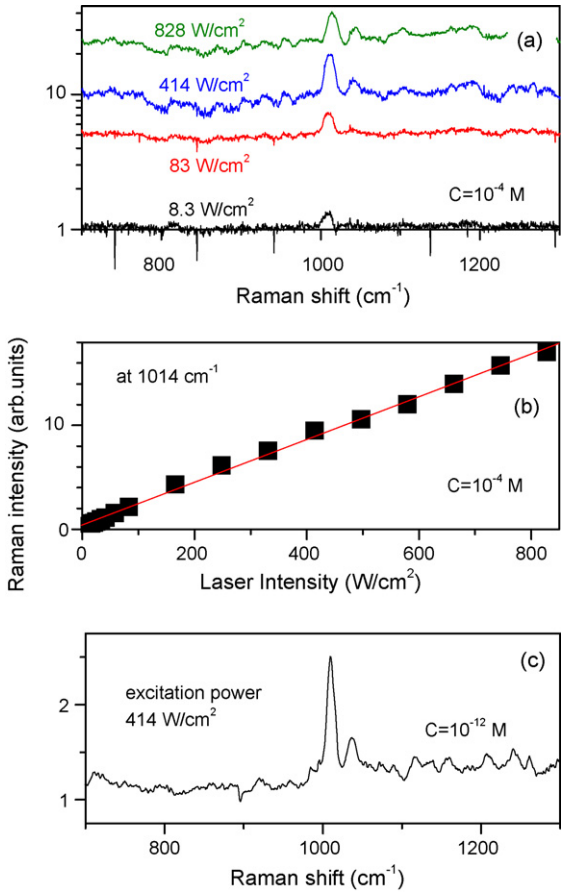

Fig. 8. (a) SERS signal from 3D textured surface (Fig. 2) immersed in 10^{-4} M pyridine solution at different excitation laser powers, (b) SERS signal dependence on the excitation power at 1014 cm^{-1} and (c) SERS signal from 10^{-12} M pyridine solution at the excitation power of 414 W/cm^2.

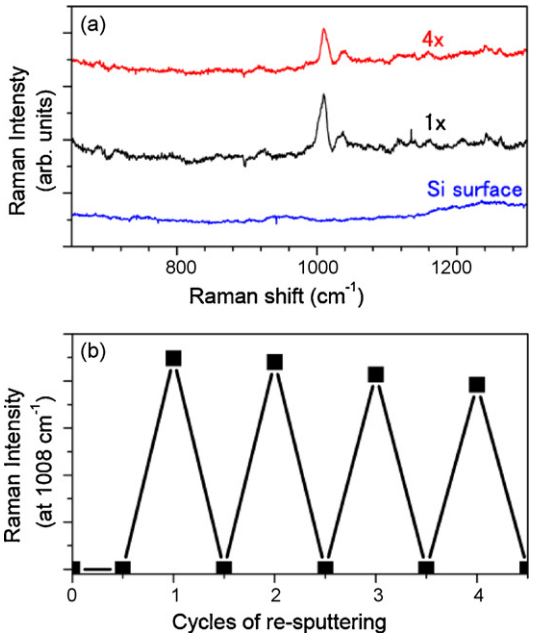

Fig. 9. (a) SERS signal from non-metalized Si surface, from as-fabricated sensor (1×), and after recycling the sensor four times (4×). Pyridine solution had the concentration of 10^{-8} M, laser excitation power was 414 W/cm^2 and (b) magnitude of SERS signal at the 1014 cm^{-1} line versus the number of wet etching and gold re-sputtering cycles.

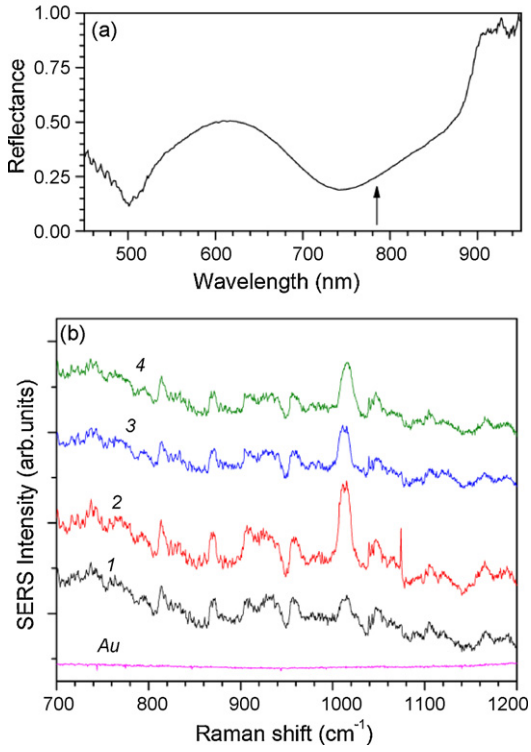

Fig. 10. (a) Reflectivity spectrum of 3D nano-structured aperture array shown in Fig. 5, (b) SERS spectra from the sample immersed in pyridine aqueous solution with the concentration of 10^{-4} M from several areas of the sample (1–4) having the same diameter (tens of nanometers). The Raman peak intensity variations are due to geometrical inhomogeneity of the sample.

where $I(\omega_l)$ is the laser intensity at the laser frequency ω_l, σ_{SERS} is the Raman scattering cross-section (usually larger than the typical Raman cross-section of 10^{-31} to 10^{-29} cm^2/molecule), and N is the number of excited Raman scatterers. Coherent Raman scattering scales proportionally to N^2, and becomes relevant when separation between the scatterers is comparable to the excitation wavelength [35]. Good linear fit of the experimental data in Fig. 8(b) by Eq. (2) signifies absence of additional unwanted non-linearities in the field enhancement factor $L(\omega_R)$. This circumstance may be helpful for quantitative SERS applications, since linear dependence of the signal on the excitation power allows pre-compensation of the signal variations due to other factors. For example, it detectable SERS signals from low concentration solutions can be obtained at moderate excitation powers as demonstrated in Fig. 8(c).

Another potential advantage of sensors having 3D structured surface geometry (see Figs. 2 and 7) is easy reusability of the sensor. Contaminated sensors are reusable after applying straightforward two-step recycling procedure: first, contaminated gold is removed by etching in I_2/NH_4I aqueous solution, and next, new gold film is deposited by sputtering. This process is technologically facile compared to the standard lift-off method which would require a lengthy electron beam drawing. The influence of sensor recycling on its sensitivity is illustrated in Fig. 9. Despite a slight degradation of the signal amplitude after the first four recycling steps (Fig. 9), it can be predictably compensated by increasing the excitation power (see Fig. 8(b)). Linearity of the sensor thus allow its operation in qualitative solute-recognition mode. Obviously, the same sensor can be used for detection of different solutes after recycling. For reliable quantitative operation, studies of the role of surface roughness and thickness of the re-sputtered Au film are necessary. These results will be reported in the future. However, the results presented above present a strong proof-of-the-principle demonstration of a reusable sensor based on SERS on a 3D nano-structured metallo-dielectric surface.

3.2. Large-area holographically defined 3D textured surface structures

Development of large-area plasmonic sensors is motivated by the possibility to augment large signals from the large sensitive area. Preparation of large-area sensors with high resolution is difficult, but it expected that the larger area will compensate for the losses that may occur due to the use of less accurate, but faster and more cost-efficient fabrication techniques. As illustrated in Section 2.2, interference patterns of two (or more) laser beams can define periodic patterns in large areas having cross-sectional diameters of the order of 1 cm, while maintaining resolution of the order of $\sim\lambda/2$, where λ is the fabrication wavelength. Using short fabrication wavelength of $\lambda < 400$ nm, achieving a resolution of about 100 nm is feasible.

Fig. 10(a) shows reflectivity spectrum of the large-area sample. The spectrum exhibits high-reflectivity region at infrared wavelengths longer than 900 nm, where incident waves see the structure as a nearly uniformly metallic effective region. At shorter wavelengths the reflectivity quickly drops, exhibiting two local minima near the wavelengths of 750 and 500 nm. Although detailed theoretical characterization of optical extinction and near-field patterns in this sample has not yet been performed, the existing literature allows to tentatively associate these minima with enhanced transmission of sub-wavelength size apertures [36,37]. Similar to metallic nano-particles, plasmonic resonances of apertures are known to be associated with enhanced near-field intensity [38], and can be thus expected to promote optical non-linear phenomena, such as SERS, at the excitation wavelength of 780 nm. Indeed, as Fig. 10(b) illustrates, detectable SERS signal from pyridine can be observed even from small areas (with diameter tens of microm-

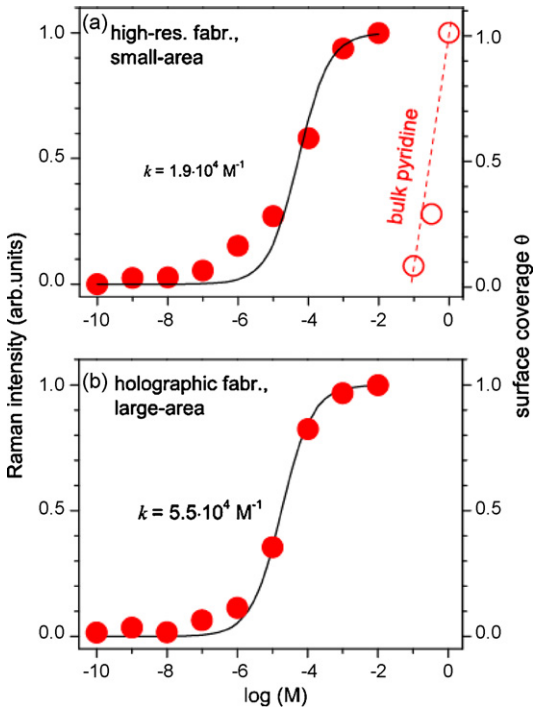

Fig. 11. Sensitivity of the small-area sensor fabricated using high resolution EBL (a), and the large-area sensor fabricated using holographic lithography (b). Solid circles represent the measured Raman signal intensity at 1014 cm^{-1} from the sensors at an excitation level of 207 W/cm^2. Open circles in (a) illustrate typical Raman signal strength obtainable from bulk pyridine solutions under similar excitation conditions. Solid lines are fit according to Eq. (3) with values of adjustable parameter k indicated in the plots.

eters) comparable to the total area of the high-resolution sensor described earlier. The Raman peak intensity varies from area to area, reflecting significant inhomogeneities existing in the sample. Despite these variations, it was verified that SERS signal integrated from the entire area is detectable at concentrations as low as 10^{-12} M at an excitation power of 414 W/cm^2 and a temporal integration window of 5 s.

3.3. Sensitivity limit of plasmonic nano-structure-based sensors

Sensitivity limit of sensors exploiting surface phenomena depends on the adsorption of solute molecules on the surface, whose sensitivity is generally assumed to be spatially uniform. Adsorption is important in predicting the achievable sensitivity, and can be characterized using Langmuir equation, which relates the surface coverage θ to the concentration of solute molecules, C [39]:

$$\theta = \theta_{\max} \frac{kC}{1 + kC}, \tag{3}$$

where $\theta_{\max}$ is the maximum coverage per area, $\theta_{\max} = 6.7 \times 10^{-18}$ mol/μm^2 for pyridine on the ⟨111⟩ gold surface [40]), and k is an adjustable parameter. Variation of the surface coverage (estimated for the horizontal surfaces only) with the solute concentration is summarized in Fig. 11. Sensitivity of both samples can be well approximated by the surface coverage parameter according to Eq. (3). In Fig. 11(a) relative strength of SERS signal from the sensor is qualitatively compared to Raman signal from bulk pyridine under similar excitation conditions. From their difference, which is approximately five orders of magnitude, and remembering that Raman scattering is proportional to I^2, one can conclude that our 3D checkerboard-type sensor can deliver local field enhancement by the factor of about 10^2. This is lower than the theoretical estimate $\sim 10^4$ obtained for the idealized model (Fig. 7), but lower parameters can be expected in real samples possessing numerous structural imperfections. Surprisingly, as Fig. 11(b) illustrates, 3D nanoaperture-based sensor, which was defined and tailored with somewhat lower resolution, also exhibits high sensitivity. In this case, large area of the sensor is most likely responsible for the strong integrated signal. It is noteworthy, that visible photo-luminescence from the gold may also be excited by the intense near-field in our sensors. The photo-luminescence, whose quantum efficiency from smooth gold surfaces is low (10^{-10} according to [1]) becomes easily detectable from gold nano-structures [7].

4. Conclusions

Optical sensors that exploit SERS effect due to plasmonic local-field enhancement were fabricated by three-dimensional nano-structuring of silicon surface with subsequent metalization by thin gold film. Two different nano-structuring techniques were used to prepare two types of sensitive surfaces. The first of them was a checkerboard pattern of 3D nanoblocks defined in compact $\sim 100\ \mu m \times 100\ \mu m$ areas of silicon wafers using EBL, and fabricated by RIE technique with subsequent metalization by gold sputtering. The second one was a square array of circular nano-apertures, defined on areas as large as $\sim 1\ cm \times 1\ cm$ using a less accurate but simpler and cheaper ultraviolet holographic lithography technique, and subsequently fabricated using a sequence of dry and wet etching as well as gold sputtering steps. These two types of sensors present an opportunity to compare optical properties, near-field enhancement and integrated SERS effects in small, precisely tailored sensors, and in large-area, less accurately tailored structures. Both kinds of the fabricated structures were found to exhibit significant near-field enhancement, as is evidenced by the strong SERS signal from sensors immersed in aqueous pyridine solutions with concentrations as low as 10^{-9} to 10^{-12} M, which was easily detectable under moderate excitation levels. Direct comparison between the sensors described here and sensors of similar type known from literature data [19,20] is difficult due to difference in the excitation intensity, wavelength, and Raman cross-section of the analyte molecules. In terms of plasmonic field enhancement, sensitivity of our structures should be regarded as moderate, since theoretical enhancement factor estimated from FDTD calculations does not exceed 10^4, which would correspond to Raman enhancement factor of about 10^8. However, in practice these values are most likely somewhat lower due to the imperfections found in the real samples. In spite of this circumstance, our sensors can deliver stable, reproducible and strong integrated SERS signals. In the small-area sample these features can be attributed to well-defined 3D periodic texture and the resulting presence of artificially tailored "hot-spots" featuring large field enhancement. On the other hand, strong SERS signal from the large-area sensor can be attributed to its larger number of active "hot-spots" which compensates for their lower field enhancement resulting from less accurate fabrication. Both kinds of sensors are versatile in terms of functionality, since their active region (surface of the gold film) can be easily recycled by chemical removal of the contaminated film and subsequent sputtering of gold, thus eliminating the need for complex EBL and lift-off procedures. Another potentially interesting possibility is to use these 3D nano-textured surfaces as molds for mass-replication of sensors using nano-imprint lithography technique. It is expected that plasmonic sensors described in this work can find practical implementation for optical sensing and detection in liquid or gaseous environments.

Acknowledgments

This work was supported by funding from the Ministry of Education, Culture, Sports, Science, and Technology of Japan: KAKENHI Grant-in-Aid for Scientific Research on the Priority Area "Strong Photons-Molecules Coupling Fields No. 470 (Nos. 19049001 and 19049016), and Grants-in-Aid from Hokkaido Innovation through Nanotechnology Support (HINTS).

References

[1] S.A. Maier, Plasmonics: Fundamentals and Applications, Springer, Berlin, 2007.
[2] E. Hutter, J. Fendler, Adv. Mater. 16 (2004) 1685–1706.
[3] R.J.C. Brown, M.J.T. Milton, J. Raman Spectrosc. 39 (2008) 1313–1326.
[4] L. Chen, J. Choo, Electrophoresis 29 (2008) 1815–1828.
[5] M. Banholzer, J. Millstone, L. Qin, C.A. Mirkin, Chem. Soc. Rev. 37 (2008) 885–897.
[6] S. Juodkazis, V. Mizeikis, H. Misawa, Adv. Polym. Sci. 213 (2008) 157–206.
[7] K. Ueno, S. Juodkazis, V. Mizeikis, K. Sasaki, H. Misawa, Adv. Mater. 20 (2008) 26–30.
[8] K. Ueno, S. Juodkazis, T. Shibuya, Y. Yokota, V. Mizeikis, K. Sasaki, H. Misawa, J. Am. Chem. Soc. 130 (2008) 6928–6929.
[9] S. Kim, J. Jin, Y.J. Kim, I.-Y. Park, Y. Kim, S. Kim, Nature 453 (2008) 757–760.
[10] H. Xu, E.J. Bjerneld, M. Käll, L. Börjesson, Phys. Rev. Lett. 83 (1999) 4357–4360.
[11] H. Xu, J. Aizpurua, M. Käll, P. Apell, Phys. Rev. E 62 (2000) 4318–4324.
[12] K. Kneipp, Y. Wang, H. Kneipp, L.T. Perelman, I. Itzkan, R.R. Dasari, M.S. Feld, Phys. Rev. Lett. 78 (1997) 1667–1670.
[13] J.A. Dieringer, R.B. Lettan II, K.A. Scheidt, R.P. Van Duyne, J. Am. Chem. Soc. 129 (2007) 16249–16256.
[14] A. Brolo, D. Irish, J. Lipkowski, J. Phys. Chem. B 101 (1997) 3906–3909.
[15] T. Wang, X. Hu, S. Dong, Small 4 (2008) 781–786.
[16] S. Mahajan, J.J. Baumberg, A.E. Russella, P.N. Bartlett, Phys. Chem. Chem. Phys. 9 (2007) 6016–6020.
[17] M.E. Abdelsalam, P.N. Bartlett, J.J. Baumberg, S. Cintra, T.A. Kelf, A.E. Russell, Electrochem. Commun. 7 (2005) 740–744.
[18] E.M. Hicks, O. Lyandres, W.P. Hall, S. Zou, M.R. Glucksberg, R.P. Van Duyne, J. Phys. Chem. C 111 (2007) 4116–4126.
[19] L.A. Dick, A.D. McFarland, C.L. Haynes, R.P. Van Duyne, J. Phys. Chem. B 106 (2002) 853–860.
[20] N.M.B. Perney, J.J. Baumberg, M.E. Zoorob, M.D.B. Charlton, S. Mahnkopf, C.M. Netti, Opt. Expr. 14 (2006) 847–857.
[21] K. Ueno, Y. Yokota, S. Juodkazis, V. Mizeikis, H. Misawa, Curr. Nanosci. 4 (2008) 232–235.
[22] K. Ueno, S. Juodkazis, V. Mizeikis, K. Sasaki, H. Misawa, J. Am. Chem. Soc. 128 (2006) 14226–14227.
[23] K. Ueno, V. Mizeikis, S. Juodkazis, K. Sasaki, H. Misawa, Opt. Lett. 30 (2005) 2158–2160.
[24] Y. Yokota, K. Ueno, V. Mizeikis, S. Juodkazis, K. Sasaki, H. Misawa, J. Nanophotonics 1 (1) (2008) 011594.
[25] K. Kinata, J. Nishii, A. Mizutani, H. Kikuta, H. Nakano, Opt. Lett. 26 (2001) 1642–1644.
[26] D.P. Dilella, H.D. Stidham, J. Raman Spectrosc. 9 (1980) 90–106.
[27] R. Dornhaus, M.B. Long, R.E. Benner, R.K. Chang, Surf. Sci. 93 (1980) 240–262.
[28] D. Rodgers, S. Luck, D. Irish, D. Guzonas, G. Atkinson, J. Electroanal. Chem. 167 (1984) 237–249.
[29] H. Raether, Surface Plasmons on Smooth and Rough Surfaces and on Gratings Springer Tracts in Modern Physics, vol. 111, Springer-Verlag, Berlin Heidelberg New York London Paris Tokyo, 1988.
[30] R. Gans, Ann. Phys. 342 (1912) 881.
[31] G. Mie, Ann. Phys. 25 (1908) 377.
[32] A. Taflove, S.C. Hagness, Computational Electrodynamics: the Finite-Difference Time-Domain Method, Artech House, 2000.
[33] P. Johnson, R. Christy, Phys. Rev. B 6 (1972) 4730–4739.
[34] M. Ordal, L. Long, R. Bell, J.R.W. Alexander, C. Ward, Appl. Opt. 22 (1983) 1099–1120.
[35] Y.B. Band, Light and Matter (Electromagnetism, Optics, Spectroscopy, and Lasers), John Wiley & Sons, Ltd., Chichester, UK, 2006.
[36] T. Ebbesen, H. Lezec, H. Ghaemi, T. Thio, P. Wolff, Nature 391 (1998) 667–669.
[37] E. Popov, S. Enoch, G. Tayeb, M. Nevière, B. Gralak, N. Bonod, Appl. Opt. 43 (2004) 999–1008.
[38] E. Popov, M. Nevière, J. Wenger, P.-F. Lenne, H. Rigneault, P. Chaumet, N. Bonod, J. Dintinger, T. Ebbesen, J. Opt. Soc. Am. A 23 (2006) 2342–2348.
[39] I. Langmuir, J. Am. Chem. Soc. 38 (1916) 2221–2295.
[40] L. Stolberg, S. Morina, J. Lipkowski, D. Irish, L. Electroanal. Chem. 307 (1991) 241–262.